Discontinuous Galerkin Finite Element Method for Euler and Navier-Stokes Equations

San-Yih Lin* and Yan-Shin Chin†

National Cheng Kung University, Tainan, Taiwan 70101, Republic of China

A finite element method for the Euler and Navier-Stokes equations has been developed. The spatial discretization involves the discontinuous Galerkin finite element method and Lax-Friedrichs flux method. The temporal discretizations used are the explicit Runge-Kutta time integrations. The scheme is formally second-order accurate in space and time. A dynamic mesh algorithm is included to simulate flows over moving bodies. The inviscid flows passing through a channel with circular arc bump, through the NACA 0012 airfoil, and the laminar flows passing over a flat plate with shock interaction are investigated to confirm the accuracy and convergence of the finite element method. Also the unsteady flow through a pitching NACA 0012 airfoil is performed to prove the capability of the present method.

I. Introduction

IN recent years, considerable progress has been made in the numerical analysis of fluid dynamics. Usually, numerical methods for aerodynamic flows, which can be solutions of Euler and Navier-Stokes equations, fall into three major classes: finite difference, finite volume, and finite element methods. Among these three methods, the finite volume method seems to be very successful in handling transonic/supersonic flows.[1-5] On the other hand, the traditional finite element method is not suitable for capturing those kinds of flows. Often, the numerical wiggles appear in the traditional finite element method computations. Hence, recently, many new ideas have been introduced in finite element methods to avoid the numerical wiggles.[5-10] Our motivation is to apply some enhancing feature, such as total variational diminishing (TVD) limiter, monotone flux, and maximum principle, in our finite element method to stabilize the scheme.

In this paper, we use a discontinuous Galerkin finite element method for the spatial discretization. The main point is that we construct three basic functions on each quadrilateral which are close to linear functions and are almost orthogonal to each other for uniform grid systems. Then, by using numerical integrations in space, we obtain three independent ordinary differential equations in time: one is to solve the mean of the flow variable, and the others are to solve the i- and j-coordinate derivatives. Because basic functions are allowed discontinuities at the interface of two quadrilaterals, an upwind technique with the Lax-Friedrich flux method is applied in the numerical procedure. Also, to avoid numerical wiggles, a local limiter is introduced to guarantee that the numerical method satisfies the maximum principle for scalar conservation laws.[11] Finally, the Runge-Kutta method is used to achieve the time marching. One may argue that the scheme is likely to require more computational time per time step than most finite difference and finite volume methods, but the scheme can easily compute the i- and j-coordinate derivatives for each dependent flow variable by integration formulas rather than use high-order interpolation/extrapolation that most finite difference and finite volume methods need to get them. Furthermore, our method can achieve high accuracy by using more information within five elements rather than using a wide range of elements, and hence it is easier to apply for boundary conditions and complicate geometries. In Ref. 11, we showed that the whole scheme is formally second-order accurate in space and time for a fixed grid system.

To simulate the flows through the NACA 0012 airfoil in arbitrary rigid body motion, a dynamic mesh algorithm[12,13] is included in our finite element method. The mesh is moved to conform to the instantaneous position of the body by modeling each edge of each quadrangle by a spring. The spring stiffness for a given edge is taken to be inversely proportional to the length of the edge. At each time step, the static equilibrium equations in the i- and j-coordinate directions are solved iteratively at each interior node of the grid for the displacements of the grid nodes. From a theoretical point of view, the dynamic grid system does not affect the accuracy of the method; but from a computational point of view, one needs to concern the geometric conservational law; how to estimate displacements of nodes and areas of quadrangle to satisfy the law is very important for keeping the accuracy of the scheme.

In this paper, to evaluate the present finite element method, several basic flow problems, such as inviscid flows passing through a channel with circular arc bump, through the NACA 0012 airfoil, and the laminar flows passing over flat plate with shock/boundary interactions, are studied. Finally, we simulate the flow passing through a pitching airfoil to prove the capability of the present method.

II. Numerical Method

A. Governing Equation

The flows of two-dimensional, compressible, and inviscid/viscous fluid can be described in conservation form by the Euler/Navier-Stokes equations

$$w_t + \nabla \cdot (f, g) = 0 \tag{1}$$

where

$$w = \begin{pmatrix} \rho \\ \rho u \\ \rho v \\ \rho e \end{pmatrix}, \quad f = \begin{pmatrix} f_1 \\ f_2 \\ f_3 \\ f_4 \end{pmatrix} = \begin{pmatrix} \rho u \\ \rho u^2 + p - \dfrac{1}{Re}\tau_{xx} \\ \rho uv - \dfrac{1}{Re}\tau_{xy} \\ u(\rho e + p) - \dfrac{1}{Re}r_4 \end{pmatrix}$$

$$g = \begin{pmatrix} g_1 \\ g_2 \\ g_3 \\ g_4 \end{pmatrix} = \begin{pmatrix} \rho v \\ \rho uv - \dfrac{1}{Re}\tau_{xy} \\ \rho u^2 + p - \dfrac{1}{Re}\tau_{yy} \\ v(\rho e + p) - \dfrac{1}{Re}s_4 \end{pmatrix}$$

with

$$\tau_{xx} = \mu(4u_x - 2v_y)/3$$

$$\tau_{xy} = \mu(u_y + v_x)$$

$$\tau_{yy} = \mu(-2u_x + 4v_y)/3$$

$$r_4 = u\tau_{xx} + v\tau_{xy} + [\mu/Pr(\gamma-1)]a_x^2$$

$$s_4 = u\tau_{xy} + v\tau_{yy} + [\mu/Pr(\gamma-1)]a_y^2$$

where p, ρ, u, v, and e are the pressure, density, x-directional velocity component, y-directional velocity component, and the total energy per unit mass, respectively. The dynamic viscosity μ is determined by Sutherland's law. The Reynolds number and Prandtl number are denoted as Re and Pr, respectively, and a is the speed of sound. The pressure p is given by the equation of state for a perfect gas

$$p = (\gamma - 1)[\rho e - 1/2\rho (u^2 + v^2)] \qquad (2)$$

where $\gamma (= 1.4$ for air) is the ratio of specific heats.

B. Space Discretization: The Discontinuous Galerkin Finite Element Method

The method used is based on a two-step modified Runge-Kutta time integration coupling with a discontinuous Galerkin finite element method. Only an outline of the numerical method is presented in Sec. II.B–II.D. A detailed development can be found in Refs. 11 and 14.

Let Ω be the computational domain of Eq. (1); $\{\Omega_{ij}\}$ a quadrilateral partition of Ω, and $\partial\Omega_{ij}$ is the boundary of Ω_{ij}. Let the approximated solution w belong to a finite dimensional space U_h and the test function V_h be the same as the space U_h such that

$$U_h = V_h = V_h^1 = \{w \in BV \cap L^1, w|_{\Omega_{ij}} \in QP^1\} \qquad (3)$$

where BV is the space of bounded variation functions, L^1 the space of L^1 integrable functions, and QP^1 the space of quasipolynomials of degree ≤ 1, which will be defined later. Note that a function in V_h^1 is allowed to have jumps at the interfaces.

Now we define the space $QP^1(\Omega)$. A function $w_h \in QP^1(\Omega)$ is given as

$$w_h(x,y;t) = \bar{w}(t) + \tilde{w}(t)\tilde{\phi}(x,y) + \tilde{\tilde{w}}(t)\tilde{\tilde{\phi}}(x,y)$$

$$(x,y) \in \Omega_{ij} \qquad (4)$$

where $\bar{w}$, $\tilde{w}$, and $\tilde{\tilde{w}}$ represent the mean, i-coordinate derivative, and j-coordinate derivative of w in Ω_{ij}, respectively. Ω_{ij} is an arbitrary quadrilateral. In Fig. 1, points A, B, C, and D are the ver-
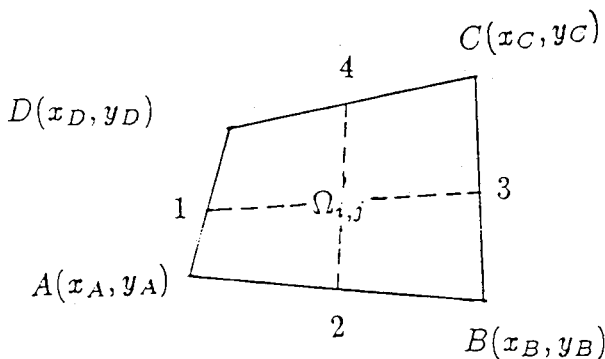

Fig. 1   Representation of quadrilateral Ω_{ij}.

tices of Ω_{ij}, and points 1, 2, 3, and 4 are the midpoints of the edges of Ω_{ij}, respectively. We choose that $\tilde{\phi}$ and $\tilde{\tilde{\phi}}$ are close to linear functions, such that

$$\tilde{\phi}(x,y) = \begin{cases} 1, & (x,y) \in \overline{BD} \\ 0, & (x,y) \in \overline{42} \\ -1, & (x,y) \in \overline{AC} \end{cases} \qquad (x,y) \in \Omega_{ij}$$

To define $\tilde{\phi}$ and $\tilde{\tilde{\phi}}$, we transform the computing quadrilateral Ω_{ij} into a square Ω' in $\xi\eta$ plane by a transform function $T(\xi,\eta)$, where $\Omega' = [(\xi,\eta), -1 \leq \xi \leq 1, -1 \leq \eta \leq 1]$. Then, we define $\tilde{\phi}$ and $\tilde{\tilde{\phi}}$ as follows:

$$\tilde{\phi}(x,y) = \tilde{\phi}[x(\xi,\eta), y(\xi,\eta)] = \tilde{\phi}'(\xi,\eta) = \xi$$

$$\tilde{\tilde{\phi}}(x,y) = \tilde{\tilde{\phi}}[x(\xi,\eta), y(\xi,\eta)] = \tilde{\tilde{\phi}}'(\xi,\eta) = \eta \qquad (5)$$

Having finished the definition of the space $QP^1(\Omega)$ and also V_h^1, we are ready to derive three ordinary differential equations for $\bar{w}$, $\tilde{w}$, and $\tilde{\tilde{w}}$ from Eq. (1). Now, multiplying Eq. (1) by $\varphi = 1$, $\varphi = \tilde{\phi}$, or $\varphi = \tilde{\tilde{\phi}}$, and integrating over an arbitrary moving subdomain $\Omega_{ij}(t)$, we can obtain (for the details, please see Refs. 11, 14, and 15):

$$\frac{d}{dt}(\bar{w}A) + \int_{\partial\Omega_{ij}(t)} (Fn_x + Gn_y)\, dl = 0 \qquad (6a)$$

$$\frac{d}{dt}\left(\frac{\tilde{w}A}{3}\right) + \int_{\partial\Omega_{ij}(t)} (Fn_x + Gn_y)\tilde{\phi}\, dl$$

$$- \int_{\Omega_{ij}(t)} (F\tilde{\phi}_x + G\tilde{\phi}_y)\, dx\, dy = 0 \qquad (6b)$$

$$\frac{d}{dt}\left(\frac{\tilde{\tilde{w}}A}{3}\right) + \int_{\partial\Omega_{ij}(t)} (Fn_x + Gn_y)\tilde{\tilde{\phi}}\, dl$$

$$- \int_{\Omega_{ij}(t)} (F\tilde{\tilde{\phi}}_x + G\tilde{\tilde{\phi}}_y)\, dx\, dy = 0 \qquad (6c)$$

where A is the area of Ω_{ij}, and n_x and n_y are unit normal vectors to the computing subdomain boundary, and

$$F = \begin{bmatrix} f_1 - \rho x_t \\ f_2 - \rho u x_t \\ f_3 - \rho v x_t \\ f_4 - \rho e x_t + p x_t \end{bmatrix}, \quad G = \begin{bmatrix} g_1 - \rho y_t \\ g_2 - \rho u y_t \\ g_3 - \rho v y_t \\ g_4 - \rho e y_t + p y_t \end{bmatrix}$$

Here x_t and y_t are the grid speeds in the x and y directions (for a fixed grid system, $x_t = y_t = 0$). For the line integrals in Eqs. (6b) and (6c), we use the following line integration formula:

$$\int_{\partial\Omega_{ij}(t)} (Fn_x + Gn_y)\varphi\, dl \sim h_{i-1/2,j}\varphi_{i-1/2,j}\bar{e}_{i-1/2,j}$$

$$+ h_{i+1/2,j}\varphi_{i+1/2,j}\bar{e}_{i+1/2,j} + h_{i,j-1/2}\varphi_{i,j-1/2}\bar{e}_{i,j-1/2}$$

$$+ h_{i,j+1/2}\varphi_{i,j+1/2}\bar{e}_{i,j+1/2} \qquad (7)$$

where $h_{i-1/2,j} = h(w_{i-1/2,j}^-, w_{i-1/2,j}^+)$ is the numerical flux at the edge $e_{i-1/2,j}$; $\bar{e}_{i-1/2,j}$ is the length of the edge; and $\varphi = 1$, $\tilde{\phi}$ or $\tilde{\tilde{\phi}}$.

And we use the local Lax-Friedrichs flux method to compute the flux h:

$$h_{i-1/2,j} = h\,(w^-_{i-1/2,j}, w^+_{i-1/2,j})$$

$$= 1/2\,\{\,F\,(w^-_{i-1/2,j})\,n_x + G\,(w^-_{i-1/2,j})\,n_y$$

$$+ F\,(w^+_{i-1/2,j})\,n_x + G\,(w^+_{i-1/2,j})\,n_y$$

$$- \alpha_{i-1/2,j}\,(w^+_{i-1/2,j} - w^-_{i-1/2,j})\,\}\qquad(8)$$

where

$$w^+_{i-1/2,j} = w^0_{i,j} - \widetilde{w}_{i,j}, \qquad w^-_{i-1/2,j} = w^0_{i-1,j} + \widetilde{w}_{i-1,j}$$

$$\alpha_{i-1/2,j} = \max_{1\le p\le m}\,(\,|\lambda^{(p)+}_{i-1/2,j}|, |\lambda^{(p)-}_{i-1/2,j}|\,)$$

and $\lambda^{p\pm}_{i-1/2,j}, p = 1,\ldots,m$, are the eigenvalues of Jacobian

$$[\,(\partial f/\partial w)\,n_x + (\partial g/\partial w)\,n_y]\,\big|_{w=w^\pm_{i-1/2,j}}$$

We note that Eqs. (6a–6c) are derived in an arbitrary moving grid system, so the value of the area A may vary with the time.

C. Runge-Kutta Time Integrations

Rewriting the system of ordinary differential equations [Eqs. (6)] as:

$$\frac{dw}{dt} = H\,(w)$$

$$w = \begin{pmatrix} w^0 \\ \widetilde{w} \\ \widetilde{\widetilde{w}} \end{pmatrix}, \qquad H\,(w) = \begin{pmatrix} \bar{H}\,(w) \\ \widetilde{H}\,(w) \\ \widetilde{\widetilde{H}}\,(w) \end{pmatrix}$$

The evolution equations are integrated in time by using the following Runge-Kutta time integrations: TVD two-step, three-step, and two-step modified Runge-Kutta methods.

1) TVD two-step Runge-Kutta integration for fixed grid systems:

$$w^{(0)} = w^n$$

$$w^{(1)} = w^{(0)} + \Delta t H\,[w^{(0)}]$$

$$w^{(2)} = w^{(1)} + \Delta t H\,[w^{(1)}]\qquad(9a)$$

$$w^{n+1} = 0.5w^{(2)} + [w^{(0)}]$$

2) Three-step Runge-Kutta integration with an under-relaxation method for computing steady-state problems:

$$w^{(0)} = w^n$$

$$\bar{w}^{(k)} = \bar{w}^{(0)} + \beta_k \cdot \Delta t \cdot \bar{H}\,[w^{(k-1)}]$$

$$\widetilde{w}^{(k)} = \widetilde{w}^{(0)} + \mu \cdot \beta_k \cdot \Delta t \cdot \widetilde{H}\,[w^{(k-1)}]\qquad(9b)$$

$$\widetilde{\widetilde{w}}^{(k)} = \widetilde{\widetilde{w}}^{(0)} + \mu \cdot \beta_k \cdot \Delta t \cdot \widetilde{\widetilde{H}}\,[w^{(k-1)}]$$

where

$$k = 1, 2, 3;\qquad \beta_1 = \alpha,\ \beta_2 = 1/2,\ \beta_3 = 1$$

$$w^{n+1} = w^{(3)}$$

where $\alpha = 0.18$ is a free parameter and $\mu = 0.09$ is a slope under-relaxation parameter. By applying the under-relaxation method on the slopes $\widetilde{w}$ and $\widetilde{\widetilde{w}}$, one can use a large Courant-Fredrichs-Lewy (CFL) number to improve the rate of convergence for computing steady-state solutions.[16]

3) Two-step modified Runge-Kutta integration for moving grid systems:

$$w^{(0)} = w^n$$

$$w^{(1)} = \frac{A^n}{A^{n+1}}\,w^{(0)} + \frac{1}{2}\frac{\Delta t}{A^{n+1}}H\,[w^{(0)}]$$

$$\qquad(9c)$$

$$w^{(2)} = \frac{A^n}{A^{n+1}}\,w^{(0)} + \frac{\Delta t}{A^{n+1}}H\,[w^{(1)}]$$

$$w^{n+1} = w^{(2)}$$

Methods 1 and 3 are second-order accurate in time and the third method includes the necessary terms to account for changes in cell areas due to the moving grids. The definitions of A^n, A^{n+1}, and x_t, y_t are presented in Sec. II.F.

D. Local Projection Limiter

To avoid the numerical wiggles at some critical points, we introduce a local projection limiter in the computing process. First we define the following local projection to limit the slopes $\widetilde{w}$ and $\widetilde{\widetilde{w}}$:

$$\widetilde{w}^{(\mathrm{mod})} = m\,(\widetilde{w}, \Delta^i_+ \bar{w}_{ij}, \Delta^i_- \bar{w}_{ij})$$

$$\widetilde{\widetilde{w}}^{(\mathrm{mod})} = m\,(\widetilde{\widetilde{w}}, \Delta^j_+ \bar{w}_{ij}, \Delta^j_- \bar{w}_{ij})\qquad(10)$$

where m is the minmod function

$$m\,(a_1, a_2, \ldots, a_n) =$$

$$\begin{cases} s \cdot \min|a_n|, & \text{if sign }(a_1) = \cdots = \text{sign }(a_n) = s \\ 0, & \text{otherwise} \end{cases}$$

and

$$\Delta^i_\pm \bar{w}_{ij} = \pm\,(\bar{w}_{i\pm 1,j} - \bar{w}_{ij})$$

$$\Delta^j_\pm \bar{w}_{ij} = \pm\,(\bar{w}_{i,j\pm 1} - \bar{w}_{ij})$$

Then define the limited values at the interface as follows:

$$w^+_{i-1/2,j} = w^0_{i,j} - \widetilde{w}^{(\mathrm{mod})}_{i,j}, \qquad w^-_{i-1/2,j} = w^0_{i-1,j} + \widetilde{w}^{(\mathrm{mod})}_{i-1,j}\qquad(11)$$

Now we plug the new interface values in Eq. (8) to compute the fluxes and to ensure that our finite element method satisfies the maximum principle for the scalar conservational laws (for the details of proof, please see Ref. 11). We note that one can use characteristic-field decompositions to define the local projection limiter to achieve a more stable scheme (see Ref. 14 for the details).

E. Boundary Conditions

We use the characteristic boundary condition to compute the far-field boundary conditions. The solid surface boundary condition for inviscid flow is no penetration, that is, the normal velocity component is zero. For viscous flow, the usual no-slip condition is applied, i.e., $u = 0, v = 0$ $(u - x_t = 0, v - y_t = 0$ for a moving grid system). The density and pressure on the wall surface, see Fig. 2 for grid structure, for inviscid and viscous flow are determined as follows:

$$\rho^b = \rho^1 - \text{minmod}\,[0.5(\rho^2 - \rho^1), \widetilde{\rho}^1]$$

$$\qquad(12)$$
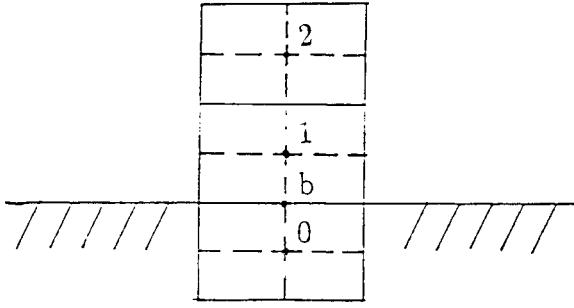
$$p^b = p^1 - 0.5(p^2 - p^1)$$

Fig. 2   Dual mesh system for boundary conditions.

F. Dynamic Grid System

In this subsection, we introduce the dynamic grid system.[12,13] The idea is that we fix the grid points on the outer boundary, correct the grid points on the inner surface boundary according to the moving body, and determine the rest of the points by modeling each edge of each cell by a spring. The spring stiffness k_{ab} for any edge a-b is taken to be inversely proportional to the length of the edge. First, we predict the displacements $\delta x_{i,j}^{(p)}$ and $\delta y_{i,j}^{(p)}$ by the following formulas:

$$\delta x_{i,j}^{(p)} = w_{i,j} \cdot \delta x_{i,1}, \quad \delta y_{i,j}^{(p)} = w_{i,j} \cdot \delta y_{i,1}, \quad j > 1 \qquad (13)$$

where $w_{i,j}$ is a smoothing weighting such that $w_{i,1} = 1$ and $w_{i,j_{max}} = 0$. The point $(i, 1)$ is on the inner surface boundary, and the point (i,j_{max}) is on the outer boundary. The $(\delta x_{i,1}, \delta y_{i,1})$ is the displacement of the inner surface point $(i, 1)$ from nth to $(n + 1)$th time. Second, we correct (or smooth) the displacements using several iterations of the equilibrium equations

$$\delta x_{i,j}^{(c)} = \frac{\sum k_m \cdot \delta x_m^{(p)}}{\sum k_m}, \quad \delta y_{i,j}^{(c)} = \frac{\sum k_m \cdot \delta y_m^{(p)}}{\sum k_m}, \quad j > 1 \qquad (14)$$

where the summations are performed over the four edges which adjoin the node (i,j). In practice, only two iterations are sufficient for our computations.

Then the new locations of the nodes can be determined by

$$x_{i,j}^{(n+1)} = x_{i,j}^{(n)} + \delta x_{i,j}^{(c)} \quad y_{i,j}^{(n+1)} = y_{i,j}^{(n)} + \delta y_{i,j}^{(c)} \qquad (15)$$

and the grid speeds x_t, y_t are determined by

$$x_t^{(n)}(i,j) = \frac{x_{i,j}^{(n+1)} - x_{i,j}^{(n-1)}}{\Delta T_1 + \Delta T_2} \quad y_t^{(n)}(i,j) = \frac{y_{i,j}^{(n+1)} - y_{i,j}^{(n-1)}}{\Delta T_1 + \Delta T_2} \qquad (16)$$

where ΔT_1 is the time step between $(n - 1)$th and nth time, and ΔT_2 between nth and $(n + 1)$th time. In each time marching process, we introduce the following geometric conservation law to calculate the area of every cell to avoid errors induced by the dynamic grid:

$$\frac{\partial}{\partial t} \int_\Omega dx\, dy - \int_{\partial \Omega} (x_t\, dy - y_t\, dx) = 0 \qquad (17)$$

And the $(n + 1)$th time cell area is determined as

$$A_{i,j}^{n+1} = A_{i,j}^n + \Delta t \sum (x_{t_m}^n \Delta y_m - y_{t_m}^n \Delta x_m) \qquad (18)$$

where the summation is taken over all edges of the cell (i,j), and Δx and Δy are determined by

$$\Delta x = \frac{\Delta x^{n+1} + \Delta x^n}{2}, \quad \Delta y = \frac{\Delta y^{n+1} + \Delta y^n}{2} \qquad (19)$$

From a theoretical point of view, the dynamic grid system does not affect the accuracy of the method. But from a computational point of view, one needs the geometric conservational law: how to estimate displacements of nodes and areas of quadrangle to satisfy the law is very important for keeping the accuracy of the scheme.
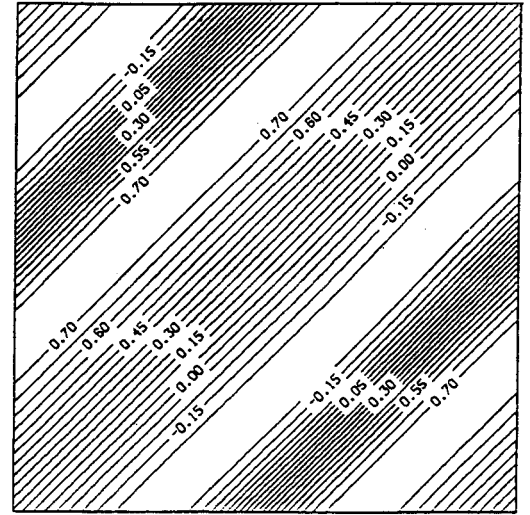
III.   Numerical Results

The approach just described is applied to compute inviscid and viscous flows through different regimes (subsonic, transonic, and supersonic flows).
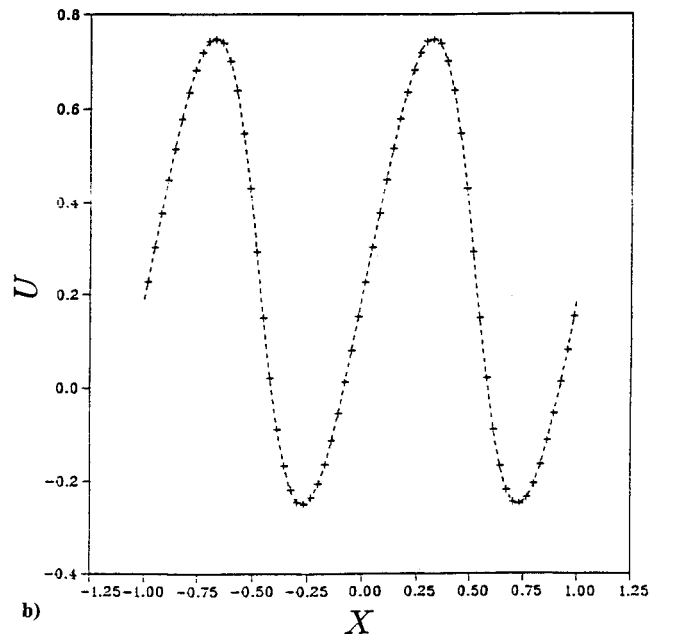
A. Scalar Burgers' Equation

To demonstrate the accuracy of the finite element method, we solve a scalar Burgers' equation

$$u_t + \left(\frac{u^2}{2}\right)_x + \left(\frac{u^2}{2}\right)_y = 0, \text{ in } (0, T) \times \Omega$$

$$\tag{20}$$

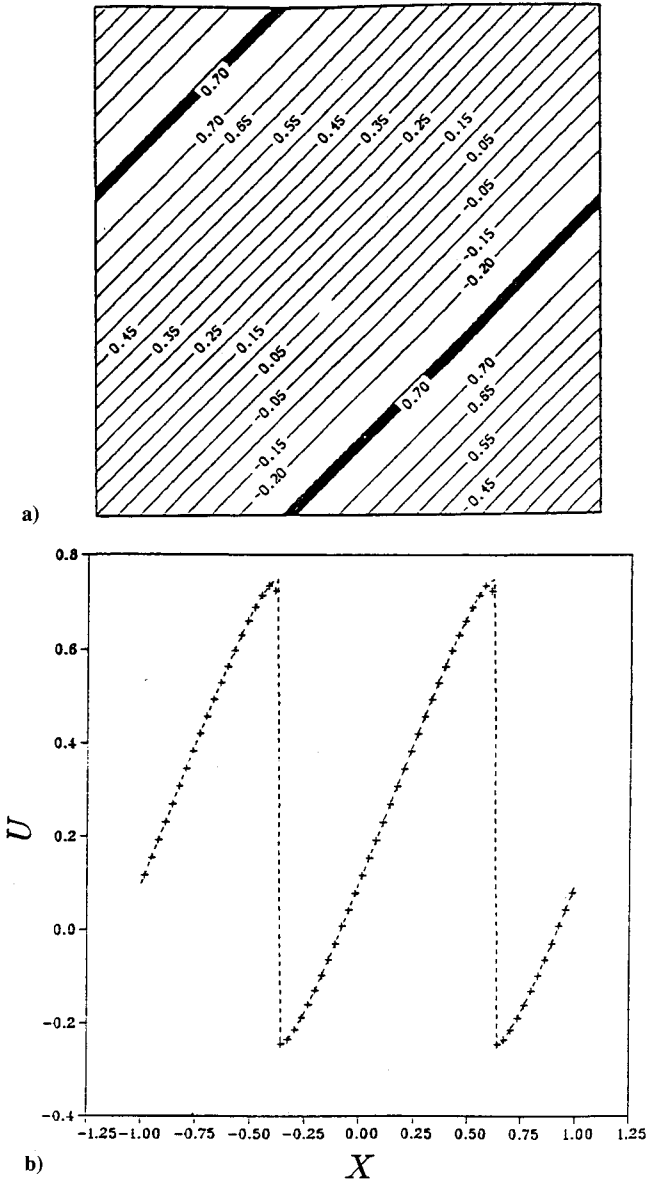$$u(x, y, 0) = \frac{1}{4} + \frac{1}{2} \sin\left[\pi(x+y)\right]$$

a)

b)

Fig. 3   Example 3.1 at $T=0.1$: a) contour of scalar solution and b) solutions along the $x = y$ line, + numerical solution and - - exact solution.
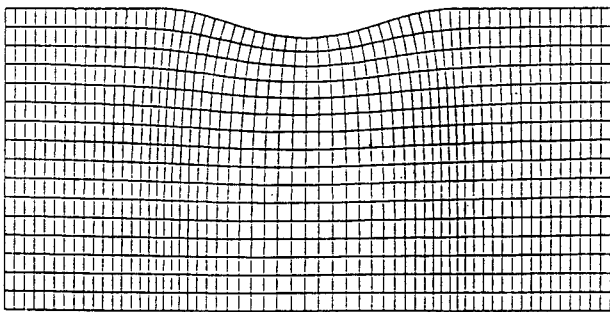
with period boundary condition, where $\Omega = (-1,1) \times (-1,1)$. Here, we solve the problem for $T = 0.1$ and 0.5 with 64×64 grid points. When $T = 0.1$, the solution is smooth and its contour is shown in Fig. 3a. The numerical solution along the line $x = y$ is shown in Fig. 3b. It can be seen that the scheme is high-order accurate and computes the extremum of the solution very well. Discontinuities develop when $T = 0.5$. The contour and numerical solution along the same line are shown in Figs. 4a and 4b. The scheme

a)

b)

Fig. 4   Example 3.1 at $T=0.5$: a) contour of scalar solution and b) solutions along the $x = y$ line, + numerical solution and - - exact solution.

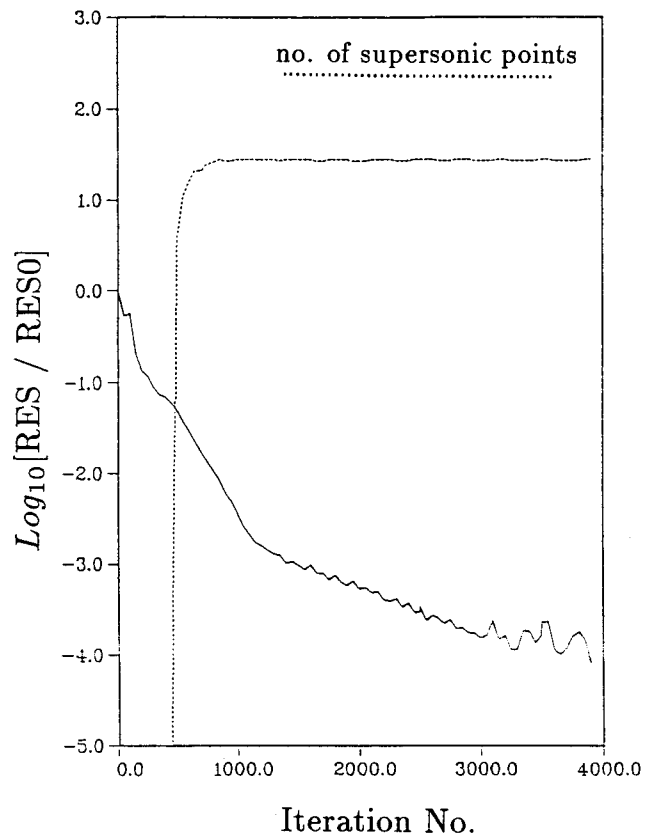**Fig. 5   Grid 61×17 for the transonic nozzle problem.**

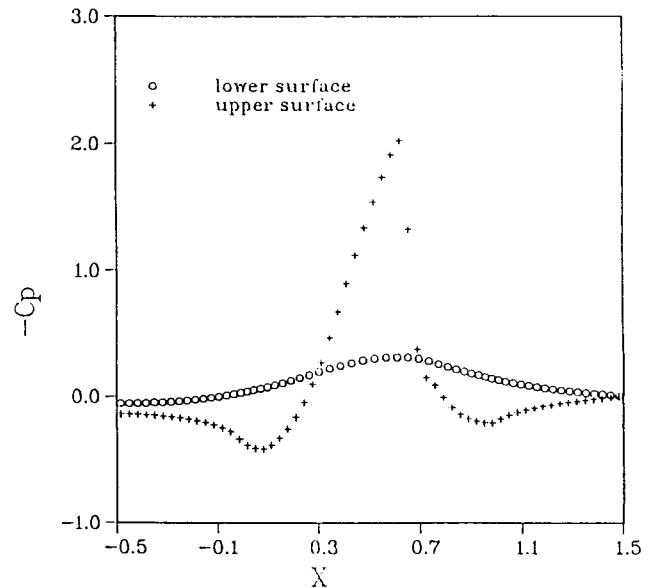**Fig. 6   Convergence history of the transonic nozzle problem.**

Fig. 7   Pressure coefficients on lower and upper surfaces.

can capture the discontinuities well. The overall results indicate that the scheme is second-order accurate in space and time (for more scalar results, please see Ref. 11).

B. Unsteady Transonic Channel Flow

In this example, we test a two-dimensional unsteady inviscid transonic channel flow with fluctuating back pressure. The channel configuration has been used for inviscid simulation by Bölcs et al.[17] The nozzle geometry consists of a channel with a (nondimensional) length of $l_l = 2.0$, with a width of $l_w = 1.0$, and with a 10% thick "bump" ($l_t/l_w = 0.10$) on the upper wall. The length of the bump is identical to the channel width.
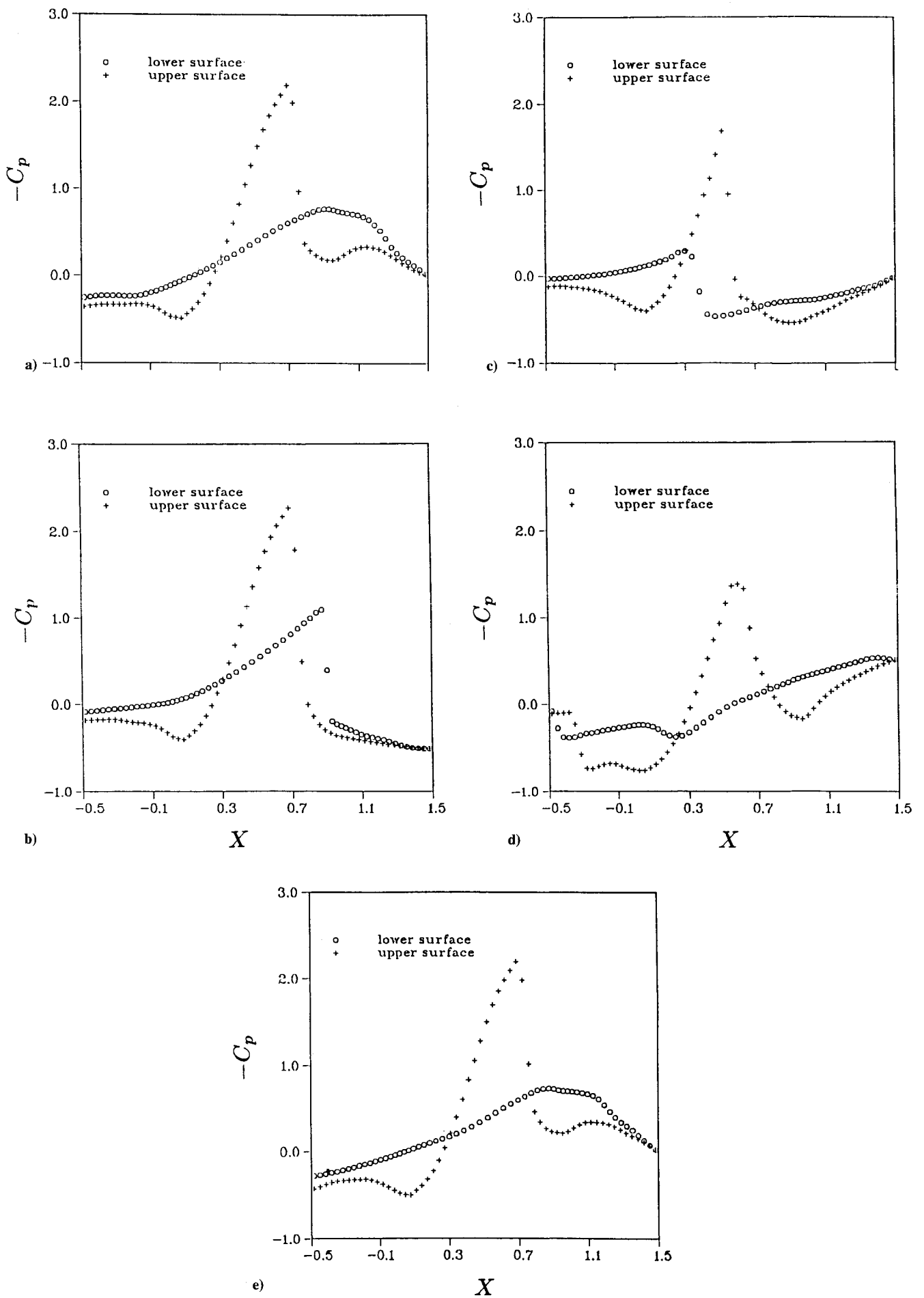
Fig. 8   Unsteady pressure coefficients: a) $t = 2\pi$, b) $t = 2.5\pi$, c) $t = 3\pi$, d) $t = 3.5\pi$, and e) $t = 4\pi$.
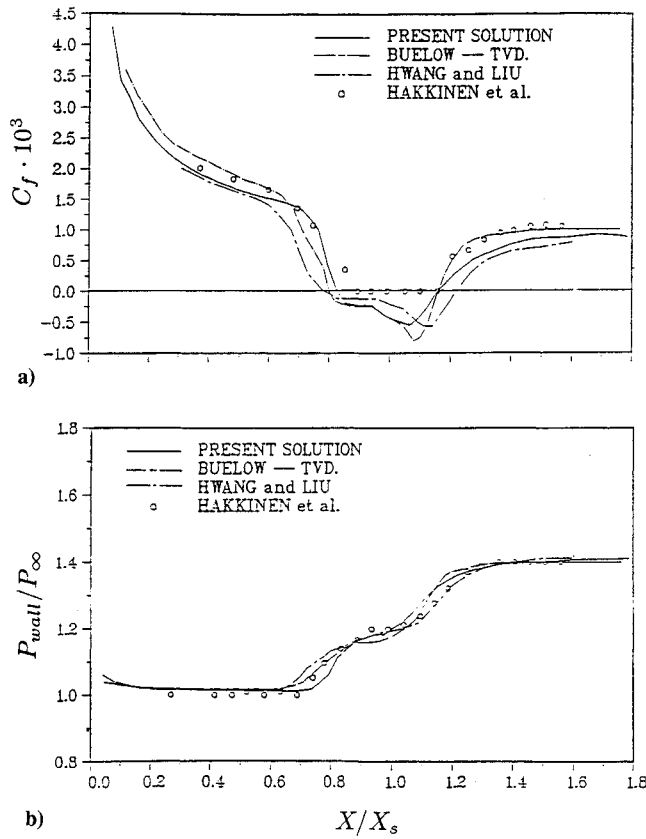
a)

b)

Fig. 9 Shock and boundary-layer interaction without bleed: a) skin friction coefficient and b) wall pressure distribution.
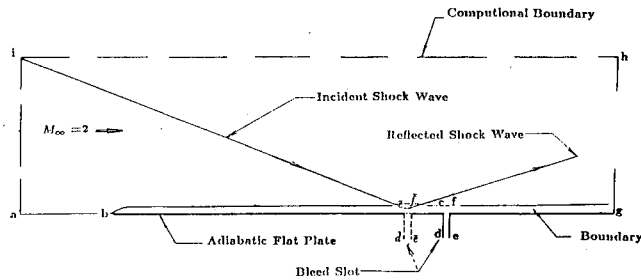

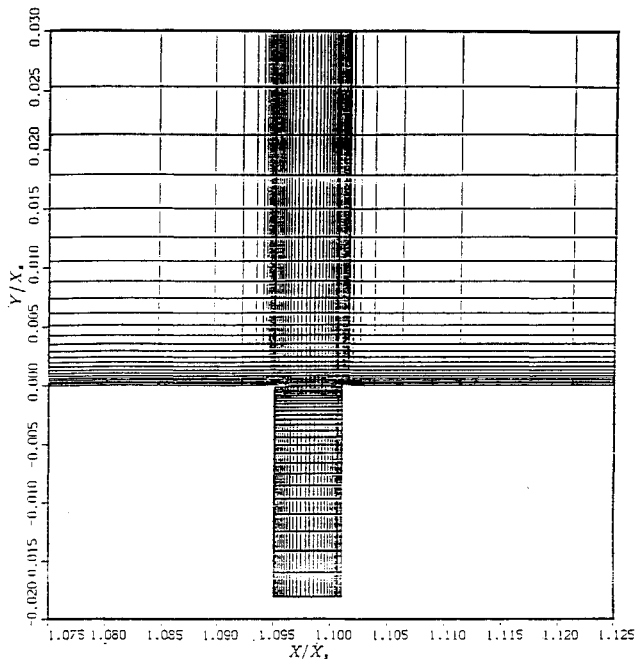**Fig. 10a Schematic of shock and boundary interaction with bleed.**

Fig. 10b Grid system.

Consider first the flow with a steady-state exit pressure of P_e/P_t = 0.7369, which corresponds to an inlet Mach number of M_∞ = 0.675. The computation grid is 61×17 and is shown in Fig. 5. The convergence history and steady-state pressure coefficient on the upper and lower surfaces are shown in Figs. 6 and 7.

Beginning from the steady-state calculation, the back pressure is varied according to a sinusoidal pressure variation

$$P = P_e + P_{e,\text{amp}} \sin [w(t - t_0)] \qquad (21)$$

where the imposed exit pressure amplitude is $P_{e,\text{amp}}/P_t$ = 0.12 with a reduced frequency of k = 0.396 (corresponding to f = 369 Hz for a channel width of l_{ref} = 0.1 m and a referenced velocity of q_{ref} = 293 m/s). Figure 8 shows the pressure coefficient distributions for one cycle. It clearly shows how the shock wave periodically moves, disappears, and reappears in the nozzle within one cycle.

C. Oblique Shock Wave/Boundary-Layer Interaction

Shock and boundary-layer interactions lead to phenomena of great complexity because of flow separation occurring.[18,19] Here we study the laminar boundary-layer interaction with an oblique shock wave. The first problem tested is the interaction of an oblique shock wave with a laminar boundary over a flat plate. The problem corresponds to the experiments of Hakkinen et al.[18] at a freestream Mach number of 2.0, shock angle of 32.6 deg, a Reynolds number based on freestream velocity, and the length from leading edge of the plate to the shock impinging point of 2.96 $\times 10^5$. The grid for this numerical experiment is the same as that used by Liou[19] and consists of 67×50 grid. Figures 9a and 9b show the skin friction coefficient and wall pressure distribution along the wall for the shock/boundary interaction without the bleed system. In the present results, an asymmetric structure is found within the shock-induced separation bubble and the negative skin friction region indicates the length of the separation bubble. It can be seen that, in the front of flow separation, the numerical result agrees well with the experimental data[18] and other numerical results.[20,21] In the region and downstream of flow separation, our result is satisfactory.

a)

b)

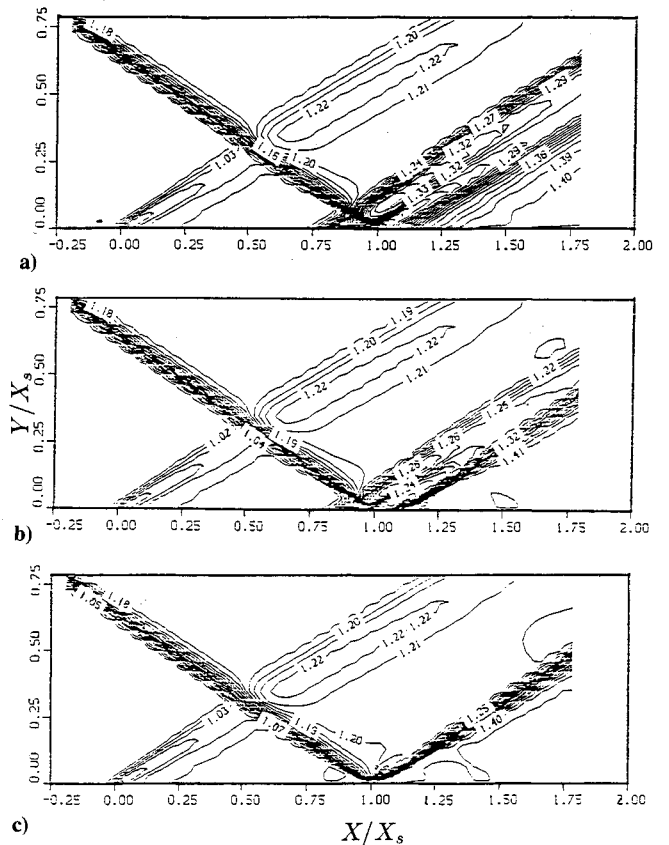c) X/X_s

Fig. 11 Pressure contours: a) without bleed, b) with bleed case 1, and c) with symmetric bleed.
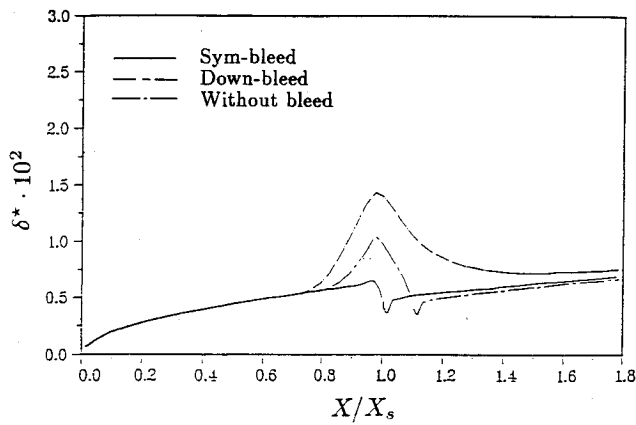
Fig. 12 Compressible displacement thickness around the shock impinging point.

Now, we proceed to study the shock and boundary-layer interactions with special attention to the boundary-layer control by using a bleed system.[22,23] Removal of the low momentum fluid near the wall, even a small mass of fluid, is capable of increasing the velocity, reducing the boundary-layer thickness, and improving the profile of the boundary layer. One of the goals is to define the optimum bleed location. Thus, in this numerical investigation, we have the following choices in determining bleed locations: 1) downstream just after the shock impinging point X_s with the slot walls at $X/X_s = 1.095$ and 1.01 (case 1, denoted down-bleed); and 2) the shock foot with the slot walls at $X/X_s = 0.997$ and 1.003 (case 2, denoted sym-bleed). Figure 10a shows the schematic of the shock wave and boundary interaction with bleed, and Fig. 10b shows the grid system. The bleed hole width and the aspect ratio (hole depth to width) are important geometric parameters in the selection of a highly efficient bleed system.[16,22] Here we fix an aspect ratio (hole depth/width) of three. For the details of this subject, please see Refs. 16, 22, and 23. Figures 11a–11c show the pressure contours
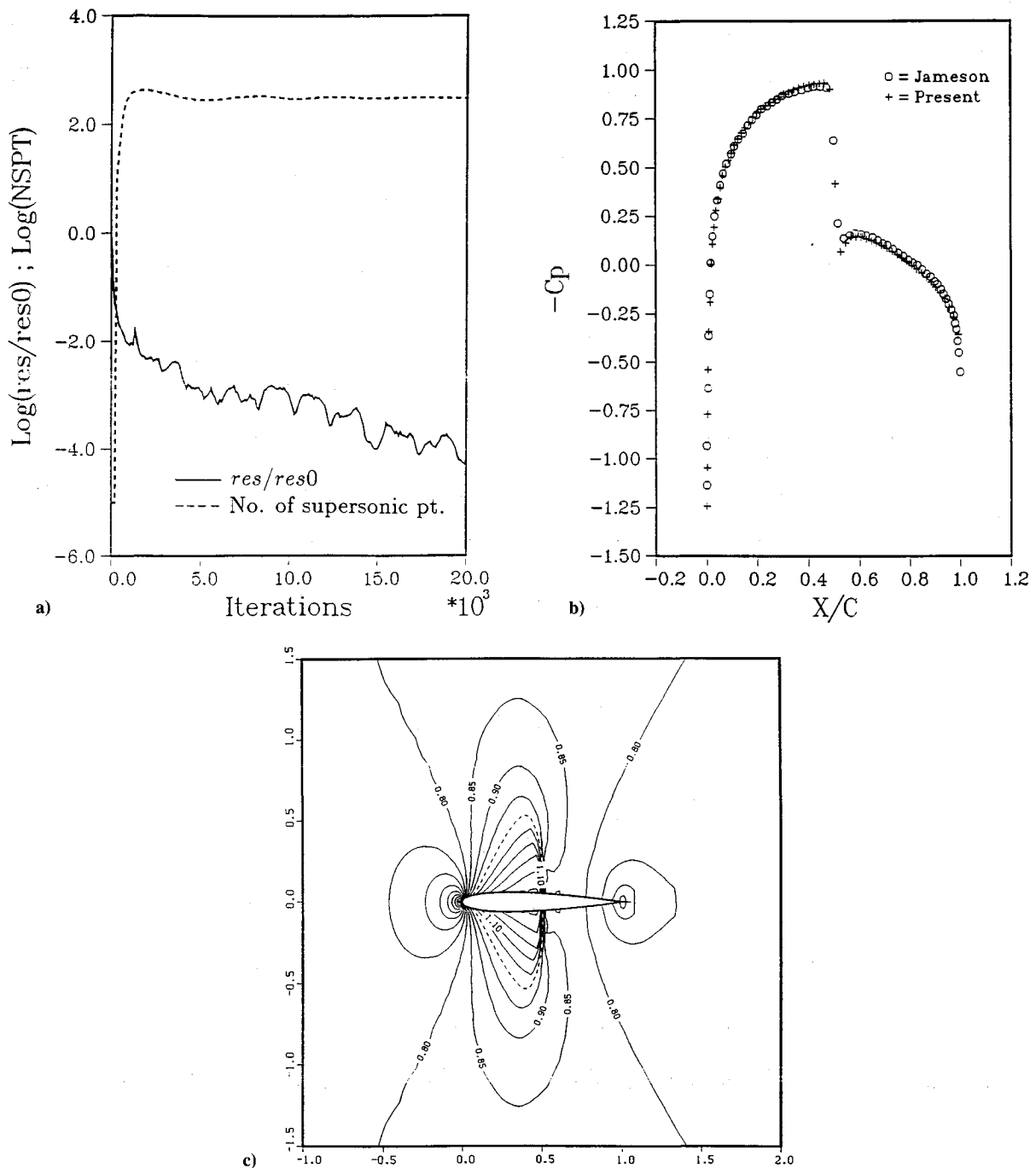

Fig. 13 Flow over NACA 0012 at Mach 2 and $\alpha = 0$: a) convergence history, b) pressure coefficients on the surfaces, and c) Mach number contour.
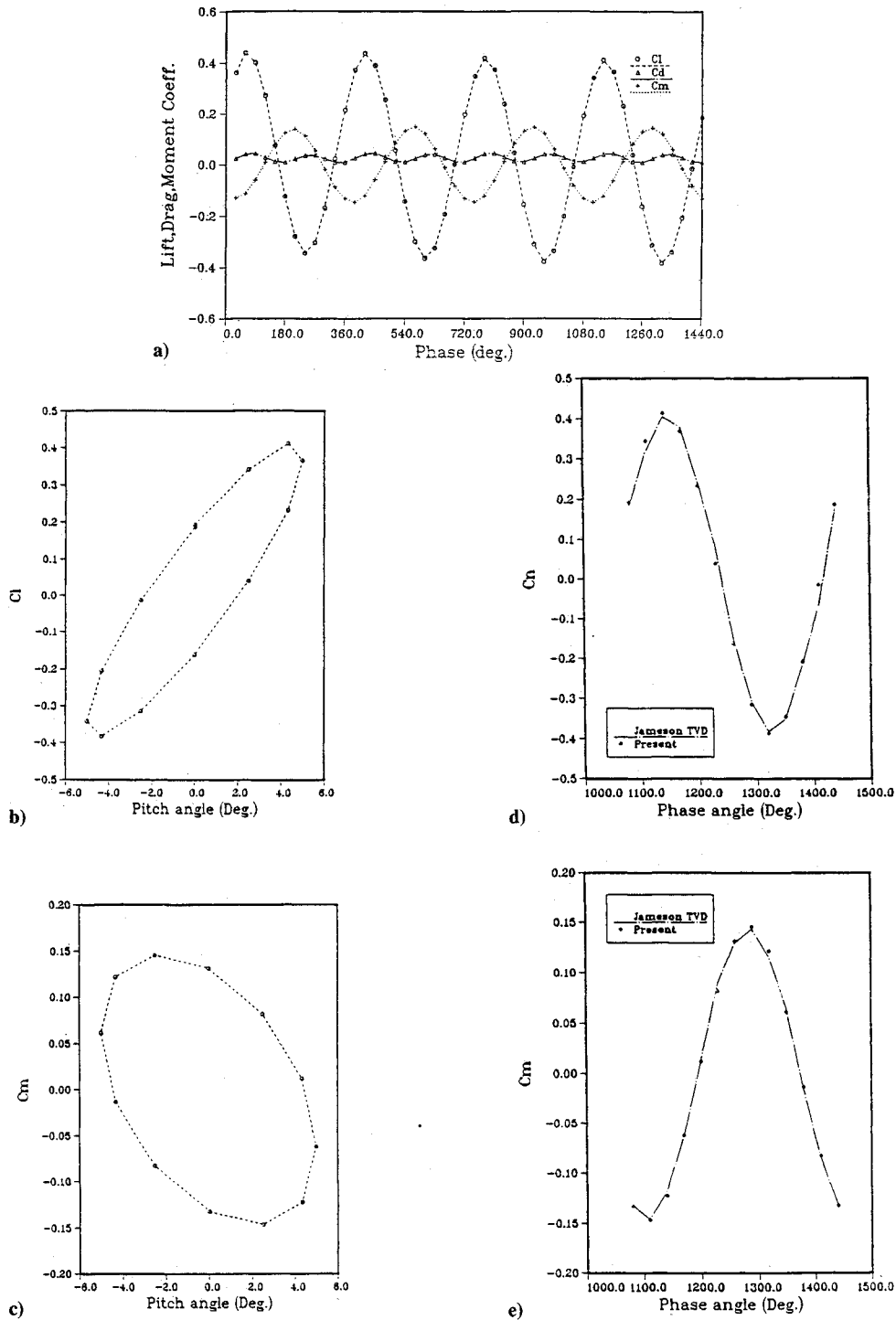
Fig. 14 Aerodynamic forces: a) variations of C_l, C_{d1}, and C_m to phase angles; b) variations of C_l to pitching angle; c) variations of C_m to pitching angle; d) coefficient of normal force; and e) coefficient of quarter-chord moment.

of the main flowfield, and Fig. 12 shows the comparisons of the compressible displacement thickness. From Fig. 11c, one can see that, under an appropriate bleed control, the main flow of shock/boundary-layer interaction is almost similar to a pure inviscid flow of shock reflection on the wall. The numerical results indicate that the position of bleed control located at the shock foot is a better choice to reduce the extent of separation region in the view of the principles of control techniques.[16]

D. Steady/Unsteady Flows Over NACA 0012 Airfoil

The problem considered is that of an NACA 0012 airfoil in a sinusoidal oscillation pitching about a fixed point at the quarter chord.[12,13,15,24,25] The angle of attack α varies according to

$$\alpha = \alpha_m + \alpha_0 \sin (2kt) \tag{22}$$

where α_m is the mean pitching angle, α_0 is the amplitude of the sinusoidal oscillation, and k is the reduced frequency.

The grid for steady/unsteady problems is C-type grid system, the minimum length on the leading edge is $\Delta x_{min} = 6.45 \times 10^{-3}$ (normalized with the chord length), on the trail edge is $\Delta x_{min} = 1.735 \times 10^{-2}$, and the minimum Δy adjacent wall surface is 7.8×10^{-3}, the computational domain expanding from the airfoil leading edge to 15 times the chord length. Figures 13a–13c show the convergence history, pressure coefficient, and Mach contour at the steady state with $\alpha = 0$ and $M_\infty = 0.8$. Figure 13b shows a comparison of pressure coefficients between our results and Jameson's results.[26] One can see differences at the leading and tail edges. We suspect that these differences may be due to the different grid structures used at those edges. By the small perturbation theory,
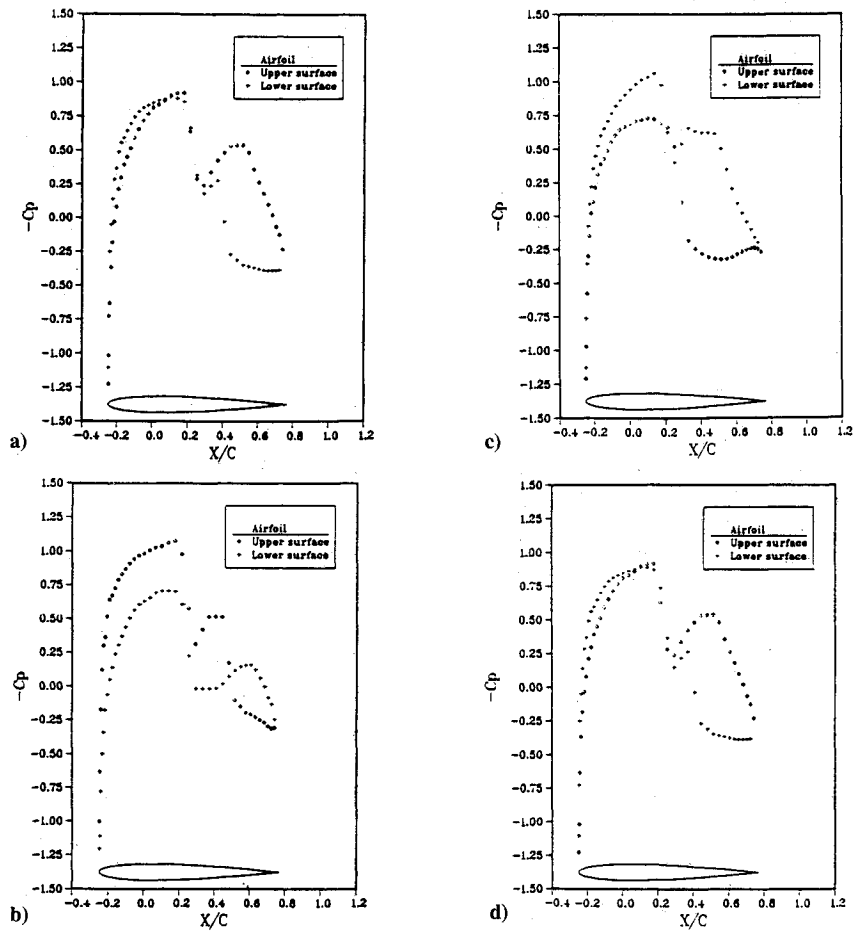
Fig. 15   Pressure coefficients on upper and lower surfaces at phase angle a) 6π, b) $40\pi/6$, c) $44\pi/6$, and d) 8π.
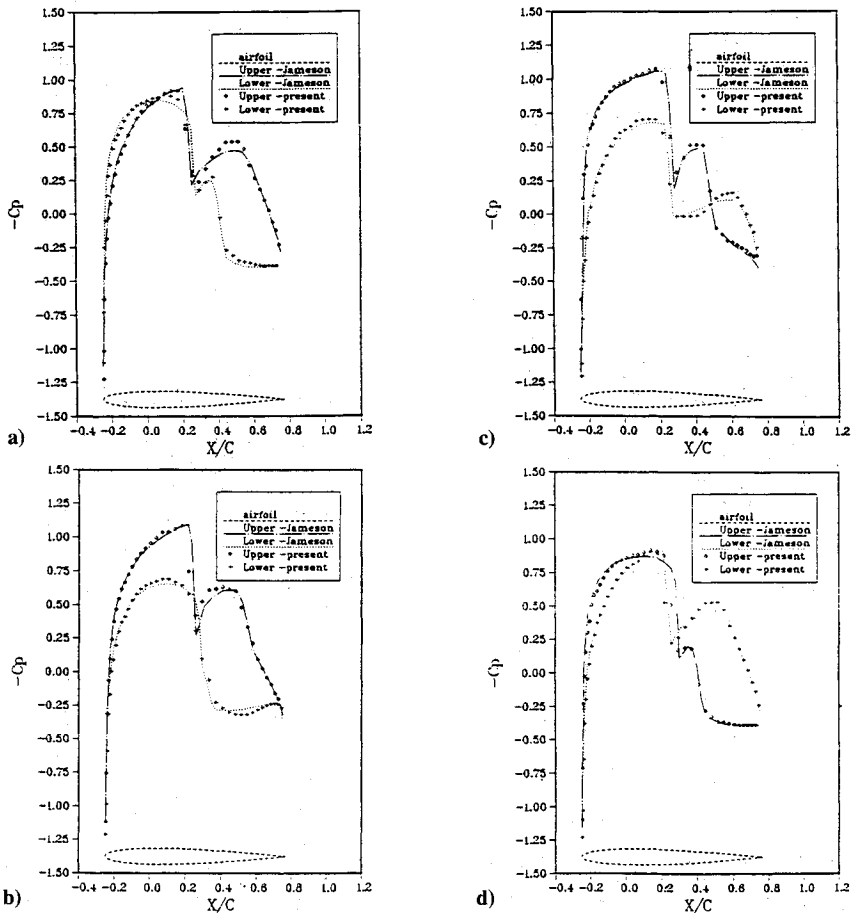

Fig. 16   Pressure coefficients on upper and lower surfaces at phase angle a) 6π, b) $38\pi/6$, c) $40\pi/6$, and d) 7π.

the maximum C_p at the leading edge is about 1.67, which indicates that our result is better at the leading edge.

For the unsteady problem, we consider $\alpha_m = 0$ deg, $\alpha_0 = 5$ deg, $k = 1$, and $M_\infty = 0.8$. Unsteady calculations are started from the convergent steady-state solution presented earlier as the initial condition. Figure 14a shows the variations of the aerodynamic forces and the quarter-chord pitching moment coefficients with phase angle $2kt$. After three cycles of pitching, C_l and C_m are almost sinusoidal. Figures 14b and 14c are the variations of C_l and C_m with pitching angle in fourth cycle, which demonstrate that the flow becomes periodic after three cycles of airfoil oscillation. Figures 14d and 14e show that the histories of normal force and pitch moment coefficients during the fourth cycle compared well with Venkatakrishnan and Jameson's results.[24] Figures 15a–15d show the surface pressure coefficient distributions during the fourth cycle. They illustrate the movement of shock waves and pressure jumps. One can see that an increase in pitching angle induces an increase of speed and shock strength on the upper surface. The reverse phenomena happens on the lower surface of the airfoil. Figures 16a–16d show the pressure coefficient distributions on airfoil surface, which agree with the Venkatakrishnan and Jameson's results.[24] The difference between our results and their results occurs at the extreme; our result of capturing extreme is sharper than theirs. This example shows that our finite element method coupling with the dynamic grid algorithm has the ability to study unsteady transonic problems with body motions.

V. Conclusion

An explicit Runge-Kutta discontinuous Galerkin finite element method for the solutions of Euler and Navier-Stokes equations has been developed. In this paper, a dynamic grid algorithm for transonic flow past an airfoil with arbitrary rigid motions is included in the numerical procedure. The accuracy and convergence of the method are investigated for some basic flows. Fairly good agreement by comparing with experimental and numerical data is observed. From the numerical results of unsteady flows over the pitching NACA 0012 airfoil and over a channel with circular arc bump, the present solution procedure is shown to be a stable and accurate approach for computing the unsteady aerodynamic flows.

Acknowledgments

References

[1]Harten, A., "High Resolution Schemes for Hyperbolic Conservation Laws," Journal of Computational Physics, Vol. 49, No. 3, 1983, pp. 357–393.

[2]Jameson, A., Baker, T. J., and Weatherill, N. P., "Calculation of Inviscid Transonic Flow over a Complete Aircraft," AIAA Paper 86-0103, Jan. 1986.

[3]Yee, H. C., "Construction of Explicit and Implicit Symmetric TVD Schemes and Their Applications," Journal of Computational Physics, Vol. 68, No. 1, 1987, pp. 151–179.

[4]Harten, A., Engquist, B., Osher, S., and Chakravarthy, S., "Uniformly High-Order Accurate Nonoscillatory Schemes, III," Journal of Computational Physics, Vol. 71, No. 2, 1987, pp. 231–303.

[5]Barth, T. J., and Jespersen, D. C., "The Design and Application of Upwind Schemes on Unstructured Meshes," AIAA Paper 89-366, Jan. 1989.

[6]Hughes, T. J., and Brooks, A., "A Theoretical Framework for Petrov-Galerkin Methods Discontinuous Weighting Functions," Finite Elements in Fluids, Vol. 4, edited by R. H. Gallagher, D. H. Norrie, J. T. Oden, and O. Z. Zienkiewics, Wiley, New York, 1982, pp. 57–65.

[7]Bristeau, M. O., Glowinski, R., Periaux, J., Perrier, P., Pironneau, O., and Poirier, G., "Transonic Flow Simulations by Finite Elements and Least-Square Methods," Finite Elements in Fluid, Vol. 4, edited by R. H. Gallagher, D. H. Norrie, J. T. Oden, and O. Z. Zienkiewics, Wiley, New York, 1982, pp. 453–482.

[8]Johnson, C., and Pitkaranta, J., "An Analysis of the Discontinuous Galerkin Method for a Scalar Hyperbolic Equation," Mathematics of Computation, Vol. 46, No. 173, 1986, pp. 1–26.

[9]Ecer, A., Akay, H. U., and Sheu, W. H., "A Variational Finite Element Formulation for Viscous Compressible Flows," Numerical Methods for Compressible Flows—Finite Difference, Element and Volume Techniques, edited by T. E. Tezduyar and T. J. R. Hughes, American Society of Mechanical Engineers, Anaheim, CA, 1986, pp. 5–17.

[10]Cockburn, B., Lin, S. Y., and Shu, C. W., "TVB Runge-Kutta Local Projection Discontinuous Galerkin Finite Element Method for Conservation Laws III: One Dimensional Systems," Journal of Computational Physics, Vol. 84, No. 1, 1989, pp. 90–113.

[11]Lin, S. Y., and Chin, Y. S., "Runge-Kutta Galerkin Finite Element Method for Two Dimensional Scalar Conservational Law," International Journal for Numerical Method in Fluids (submitted for publication).

[12]Batina, J. T., "Unsteady Euler Airfoil Solution Using Unstructured Dynamic Meshes," AIAA Journal, Vol. 28, No. 8, 1990, pp. 1381–1388.

[13]Lin, C. Y., "Transonic Full Potential Calculation of Oscillating Airfoil Flow," M.S. Thesis, Inst. of Aeronautics and Astronautics, National Cheng Kung Univ., Tainan, Taiwan, ROC, June 1989.

[14]Chin, Y. S., "Unsteady Transonic Flow Computation by Finite Element Method," M.S. Thesis, Inst. of Aeronautics and Astronautics, National Cheng Kung Univ., Tainan, Taiwan, ROC, June 1990.

[15]Wang, Y. Y., "Numerical Investigations on Airfoil Performance Subjected to Aerodynamic Interference from an Upstream Airfoil," M.S. Thesis, Inst. of Aeronautics and Astronautics, National Cheng Kung Univ., Tainan, Taiwan, ROC, June 1992.

[16]Dung, Y. F., "A Numerical Investigation of Shock Wave/Boundary Layer Interaction by Finite Element Method," M.S. Thesis, Inst. of Aeronautics and Astronautics, National Cheng Kung Univ., Tainan, Taiwan, ROC, June 1991.

[17]Bölcs, A., Fransson, T. H., and Platzer, M. F., "Numerical Simulation of Inviscid Transonic Flow Through Nozzles with Fluctuating Back Pressure," Transactions of the ASME, Journal of Turbomachinery, Vol. 111, No. 2, 1989, pp. 169–180.

[18]Hakkinen, R. J., Greber, I., Trilling, L., and Arbarbanel, S. S., "The Interaction of an Oblique Shock Wave with a Laminar Boundary Layer," NASA Memo-2-18-59, March 1959.

[19]Liou, M. S., "A Newtom Upwind Method and Numerical Study of Shock Wave and Boundary Layer Interaction," International Journal for Numerical Method in Fluids, Vol. 9, No. 7, 1989, pp. 747–761.

[20]Buelow, P. E., "Comparison of TVD Schemes Applied to the Navier-Stokes Equations," AIAA Paper 89-0847, Jan. 1989.

[21]Hwang, C. J., and Liu, J. L., "Inviscid and Viscous Solutions for Airfoil/Cascade Flows Using a Locally Implicit Algorithm on Adaptive Meshes," ASME Journal of Turbomachinery, Vol. 113, No. 4, 1991, pp. 553–560.

[22]Syberg, J., and Koncsek, J. L., "Bleed System Design Technology for Supersonic Inlet," AIAA Paper 72-1138, Nov. 1972.

[23]Holdon, M. S., "Shock Wave-Turbulent Boundary Layer Interaction in Hypersonic Flow," AIAA Paper 75-45, Jan. 1975.

[24]Venkatakrishnan, V., and Jameson, A., "Computation of Unsteady Transonic Flows by the Solution of Euler Equations," AIAA Journal, Vol. 26, No. 8, 1988, pp. 974–981.

[25]Hong, C. C., "Finite Element Computation of Unsteady Transonic Flow Past Airfoil," M.S. Thesis, Inst. of Aeronautics and Astronautics, National Cheng Kung Univ., Tainan, Taiwan, ROC, June 1991.

[26]Jameson, A., "Numerical Solutions of the Euler Equations by Finite Volume Methods Using Runge-Kutta Time-Stepping Schemes," AIAA Paper 81-1259, June 1981.